44th AIAA/ASME/SAE/ASEE Joint Propulsion Conference & Exhibit
21 - 23 July 2008, Hartford, CT

AIAA 2008-5021

Energy Based Mean Flow Solutions for Slab Hybrid Rocket Chambers

Tony Saad* and Joseph Majdalani†
University of Tennessee Space Institute, Tullahoma, TN 37388

In a recent study, Taylor's incompressible model for a porous cylinder was generalized to account for energy-triggered solutions with arbitrary headwall injection (Majdalani and Saad, "Energy Steepened States of the Taylor-Culick Profile," AIAA Paper 2007-5797, July 2007). In this sequel, we extend the analysis to the planar configuration while incorporating arbitrary headwall injection. Using a porous channel to model a slab hybrid chamber, we introduce Lagrangian multipliers and optimize the total kinetic energy of the system. The Lagrangian optimization principle yields mean flow solutions that depend on the chamber aspect ratio as well as the headwall injection profile and a quantum-like energy power index, *q*. Subsequently, the resulting solutions are classified according to their energy content with reference to Taylor's basic solution. Physically, what we dub the Type I families of solutions exhibit steeper profiles and energy levels that are lower than Taylor's. Conversely, the Type II families exhibit smoother profiles with energy levels that exceed Taylor's. Both types approach Taylor's expression as their energy power index *q* is increased.

Nomenclature

a	= chamber half height
E_V	= total volumetric kinetic energy
$\mathscr{E}$	= kinetic energy density, E_V / L^3
$\boldsymbol{u}$	= normalized velocity $(\bar{u}, \bar{v})/U_w$
U_c	= headwall injection velocity, $\bar{u}(0,0)$
u_c	= normalized injection velocity, U_c / U_w
U_w	= sidewall injection velocity, $-\bar{v}(\bar{x}, a)$
x, y	= normalized axial and vertical coordinates, $\bar{x}/a$, $\bar{y}/a$
η	= action variable, $(n+\frac{1}{2})\pi y$
ν	= kinematic viscosity, μ/ρ
ρ	= density

Symbols

c	= centerline property
h	= headwall property
w	= sidewall property
$\bar{}$	= overbars denote dimensional variables
$^-$	= a superscripted minus denotes Type I solutions
$^+$	= a superscripted plus denotes Type II solutions

I. Introduction

TAYLOR's solution for an injection-driven porous channel was derived under the assumptions of steady, inviscid, incompressible, rotational and pseudo-viscous conditions.[1] Despite its inviscid origin, its streamlines

*Doctoral Research Assistant, Department of Mechanical, Aerospace and Biomedical Engineering. Member AIAA.
†H. H. Arnold Chair of Excellence in Advanced Propulsion, Department of Mechanical, Aerospace and Biomedical Engineering. Member AIAA. Fellow ASME.

observed the no slip requirement along the porous sidewalls.[2] In recent work, Majdalani and Saad[3] presented a closed-form rotational solution for the axisymmetric Taylor-Culick profile with arbitrary headwall injection as well as for the porous channel case with arbitrary injection (Saad and Majdalani[4]). Their models were suitable for describing the bulk fluid motion in cylindrical and slab rocket chambers with either solid or hybrid grains. They also extended the Taylor-Culick flow by developing energy dependent approximations that could display either steeper or smoother velocity profiles.[5] Their analysis suggested the possible establishment of a continuous spectrum of solutions each bearing a different kinetic energy signature (see Apte and Yang[6,7]).

In this article, we follow similar lines and procure energy based solutions for the injection-driven porous channel. In the process, we construct approximate solutions that satisfy the problem's constraints while either minimizing or maximizing the system's energy. After bracketing the limiting solutions for several headwall injection profiles, we compare and classify two distinct families of solutions (Types I and II) depending on their energy content. In all of the cases considered, simple approximations are produced for sufficiently long chambers.

Extending our analysis to the planar configuration serves two main objectives. Not only does it prescribe a new method of approximation for mean flow fields but also carries the advantage of providing an avenue for comparison with experimental and numerical profiles associated with slab burner grains in both hybrid and solid rocket chambers. These are becoming increasingly more common in propulsion related simulations.[6-8] Finally, the reduced complexity of the Cartesian case provides a simple platform for delving into the physical mechanisms that are intrinsic to two-dimensional flows through porous channels.

II. Mathematical Model

The slab motor can be modeled as a porous channel of length L_0 and height $2a$. We also permit the forward end to be porous while assuming an open aft end. As shown in Fig. 1, $\bar{x}$ and $\bar{y}$ represent the axial and normal coordinates, respectively. Note that the porous headwall permits the injection of a fluid at a user-defined velocity profile, $\bar{u}_0(\bar{y})$. Special cases of $\bar{u}_0(\bar{y})$ include

$$\bar{u}_0(\bar{y}) = \bar{u}(\bar{y},0) = \begin{cases} U_c = \text{const}; & \text{uniform} \\ U_c \cos(\pi \bar{y} / 2a); & \text{sinusoidal} \\ U_c[1-(\bar{y}/a)^m]; & \text{laminar and turbulent} \end{cases} \tag{1}$$

Our solution domain extends from the headwall to the parallel, virtual nozzle attachment plane at the aft end.

At the headwall, an axial jet enters the chamber at a maximum centerline speed, U_c. This stream is then augmented by uniform mass addition along the porous sidewall. In what follows, we seek to approximate other solutions that may exist besides Taylor's basic relation. In particular, we hope to identify those particular solutions that require the least or most energy to excite.

A. Equations

An inert flow may be assumed, prompted by the typically thin reactive zone above the grain surface. Following rote, the basic flow can be taken to be steady, inviscid, incompressible, rotational, and axisymmetric. Euler's equations become

$$\frac{\partial \bar{u}}{\partial \bar{x}} + \frac{\partial \bar{v}}{\partial \bar{y}} = 0 \tag{2}$$

$$\bar{u}\frac{\partial \bar{u}}{\partial \bar{x}} + \bar{v}\frac{\partial \bar{u}}{\partial \bar{y}} = -\frac{1}{\rho}\frac{\partial \bar{p}}{\partial \bar{x}} \tag{3}$$

$$\bar{u}\frac{\partial \bar{v}}{\partial \bar{x}} + \bar{v}\frac{\partial \bar{v}}{\partial \bar{y}} = -\frac{1}{\rho}\frac{\partial \bar{p}}{\partial \bar{y}} \tag{4}$$

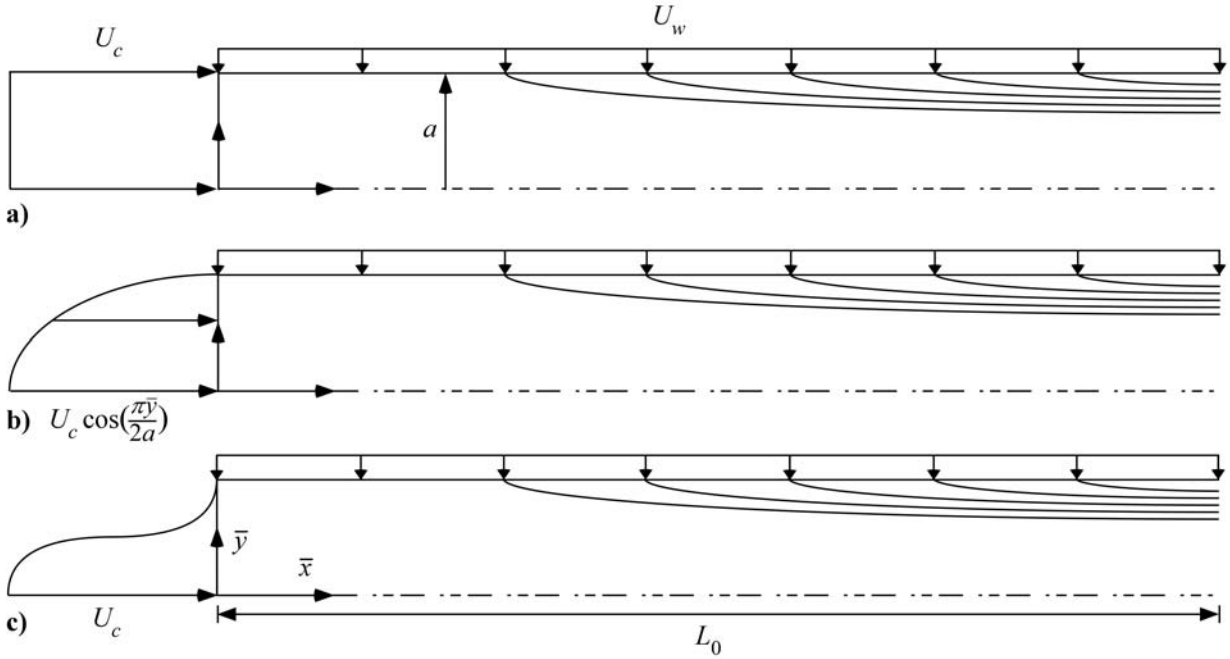

Figure 1. Simulated slab rocket as a porous channel with arbitrary headwall injection.

B. Boundary Conditions

These are physically connected to

(a) axial symmetry and therefore no flow across the midsection plane;
(b) vanishing axial flow at the sidewall to secure the no slip boundary condition;
(c) uniform injection at the sidewall; and
(d) a user-prescribed injection pattern at the headwall.

Mathematically, these particulars can be written as

$$\begin{cases} \text{(a)}\ \ \bar{v}(\bar{x},0)=0 & \text{(no flow across midsection plane)} \\ \text{(b)}\ \ \bar{u}(0,\bar{y})=U_0(\bar{y}) & \text{(headwall injection profile)} \\ \text{(c)}\ \ \bar{v}(\bar{x},\pm 1)=-U_w & \text{(constant sidewall mass addition)} \\ \text{(d)}\ \ \bar{u}(\bar{x},1)=0 & \text{(no slip)} \end{cases} \tag{5}$$

C. Normalization

All variables and operators may be normalized using the following definitions:

$$x=\frac{\bar{x}}{a};\ y=\frac{\bar{y}}{a};\ \nabla=a\bar{\nabla};\ p=\frac{\bar{p}}{\rho U_w^2};\ \psi=\frac{\bar{\psi}}{aU_w};\ \boldsymbol{\Omega}=\frac{\bar{\boldsymbol{\Omega}}a}{U_w} \tag{6}$$

$$u=\frac{\bar{u}}{U_w};\ v=\frac{\bar{v}}{U_w};\ u_0=\frac{U_0}{U_w};\ u_c=\frac{U_c}{U_w};\ L=\frac{L_0}{a} \tag{7}$$

Here $U_c=\bar{u}(0,0)$ and $U_w=-\bar{v}(\bar{x},a)$ designate the fluid injection velocities at the headwall and sidewall, respectively. For steady inviscid motion, the vorticity transport equation reduces to

$$\nabla\times\boldsymbol{u}\times\boldsymbol{\Omega}=0\ ;\quad \boldsymbol{\Omega}=\nabla\times\boldsymbol{u} \tag{8}$$

Similarly, the dimensionless boundary conditions take the form

$$\text{(a)}\ \ v(x,0)=0;\qquad \text{(b)}\ \ u(0,y)=u_0(y);\qquad \text{(c)}\ \ v(x,1)=-1;\qquad \text{(d)}\ \ u(x,1)=0 \tag{9}$$

Due to symmetry at the midsection plane, we consider only half of the channel.

D. Vorticity-Stream Function Decomposition

The Stokes stream function may be introduced through

$$u = \frac{\partial \psi}{\partial y} \quad \text{and} \quad v = -\frac{\partial \psi}{\partial x} \tag{10}$$

As usual,[3,4] substitution into Eq. (8) requires

$$\Omega = \Omega_z = F(\psi) \tag{11}$$

One then follows tradition[1] and selects the simplest relation between Ω and ψ, namely,

$$\Omega = K^2 \psi \tag{12}$$

Despite the non-uniqueness of this expression, it permits securing Eq. (8). By inserting Eq. (12) into the vorticity equation, one eliminates Ω and restores the PDE characteristic of this problem. This is

$$\nabla^2 \psi + K^2 \psi = 0 \tag{13}$$

Its particular set of constraints comprise:

$$\frac{\partial \psi(x,0)}{\partial x} = 0 \quad \text{(a)}; \quad \frac{\partial \psi(x,1)}{\partial x} = 1 \quad \text{(b)}; \quad \frac{\partial \psi(0,y)}{\partial y} = u_0(y) \quad \text{(c)}; \quad \frac{\partial \psi(x,1)}{\partial y} = 0 \quad \text{(d)} \tag{14}$$

Equation (13) may be solved by separation of variables; one finds

$$\psi(x,y) = (\alpha x + \beta)[A\cos(Ky) + B\sin(Ky)]. \tag{15}$$

III. Energy Based Solutions

A. Solution by Eigenfunction Expansions

The application of the boundary conditions is carried out in the order in which they appear. Starting with Eq. (14)a, we have

$$\frac{\partial \psi(x,0)}{\partial x} = \alpha A\cos(Ky) + \alpha B\sin(Ky)\big|_{y=0} = 0 \tag{16}$$

or $A = 0$. Without loss in generality, we set $B = 1$ and rewrite Eq. (14)b as

$$\frac{\partial \psi}{\partial y}(x,1) = K(\alpha x + \beta)\cos(K) = 0 \ \text{ or } \ \cos(K) = 0 \tag{17}$$

This condition is satisfied when

$$K_n = (n + \tfrac{1}{2})\pi \quad \forall n \in \{0,1,2,3,...,\infty\} \tag{18}$$

Using $K_n = (n+\frac{1}{2})\pi$ enables us to sum over eigenfunctions to construct the total solution. Ignoring negative integers to avoid self-cancellation, one can put

$$\psi_n = (\alpha_n x + \beta_n)\sin\left[\left(n+\tfrac{1}{2}\right)\pi y\right] \quad \text{or} \quad \psi(x,y) = \sum_{n=0}^{\infty}(\alpha_n x + \beta_n)\sin\left[\left(n+\tfrac{1}{2}\right)\pi y\right] \tag{19}$$

The headwall boundary condition may be satisfied by means of orthogonality; one recovers, for an injection profile $u_0(y)$, the following compact form:

$$\beta_n = \frac{4}{(2n+1)\pi}\int_0^1 u_0(y)\cos[(n+\tfrac{1}{2})\pi y]\,\mathrm{d}y \tag{20}$$

When evaluated for several injection profiles, we obtain

$$\beta_n = \begin{cases} 0; & u_0(y) = 0 \\ \dfrac{(-1)^n 8u_c}{\pi^2(2n+1)^2}; & u_0(y) = u_c \\ 2\dfrac{u_c}{\pi}; \ \ n=0 \quad (0; \ \forall n \neq 0); & u_0(y) = u_c\cos\left(\tfrac{1}{2}\pi y\right) \\ \dfrac{(-1)^n 64u_c}{\pi^4(2n+1)^4}; & u_0(y) = u_c\left(1-y^2\right) \end{cases} \tag{21}$$

The third condition becomes

$$\frac{\partial \psi}{\partial x}(x,1) = \sum_{n=0}^{\infty}\alpha_n \sin\left[\left(n+\tfrac{1}{2}\right)\pi\right] = 1 \quad \text{or} \quad \sum_{n=0}^{\infty}(-1)^n\alpha_n = 1 \tag{22}$$

Clearly, an infinite number of possibilities exist that would, in principle, satisfy Eq. (22), depending on the behavior of the sidewall injection sequence $\{\alpha_n\}$.

B. Kinetic Energy Optimization

One of the choices for $\{\alpha_n\}$ may be arrived at by optimizing the total kinetic energy in the chamber. The underlying principle projects that a flow may choose the path of least or most energy expenditure. To test this behavior, we evaluate the local kinetic energy at (x, y, z) for each eigensolution. We let

$$E_n(x, y, z) = \tfrac{1}{2}\boldsymbol{u}_n^2 = \tfrac{1}{2}(u_n^2 + v_n^2 + w_n^2) \tag{23}$$

where each mode is an exact solution bearing the form

$$\begin{cases} u_n = K_n(\alpha_n x + \beta_n)\cos\eta \\ v_n = -\alpha_n \sin\eta \quad w_n = 0 \end{cases}; \quad \eta = \left(n + \tfrac{1}{2}\right)\pi y \tag{24}$$

By assuming a system of eigensolutions with individual kinetic energies, their cumulative sum can be written locally as

$$E\left(x, y, z\right) = \sum_{n=0}^{\infty} E_n\left(x, y, z\right) = \tfrac{1}{2}\sum_{n=0}^{\infty}\left[K_n^2(\alpha_n x + \beta_n)^2\cos^2\eta + \alpha_n^2\sin^2\eta\right] \tag{25}$$

The total kinetic energy in the chamber volume V may be calculated by integrating the local kinetic energy over the length and chamber cross-section, assuming unit depth. One puts

$$E_V = \int_{-\frac{1}{2}}^{\frac{1}{2}}\int_{-1}^{1}\int_{0}^{L} E\,\mathrm{d}x\,\mathrm{d}y\,\mathrm{d}z = \tfrac{1}{2}\sum_{n=0}^{\infty}\int_{-1}^{1}\int_{0}^{\mathrm{L}}\left[K_n^2(\alpha_n x + \beta_n)^2\cos^2\eta + \alpha_n^2\sin^2\eta\right]\mathrm{d}x\,\mathrm{d}y \tag{26}$$

Straightforward evaluation and simplification over the chamber volume yields

$$E_V = \tfrac{1}{6}L^3\sum_{n=0}^{\infty} a_n\alpha_n^2 + b_n\alpha_n L^{-1} + c_n L^{-2} + 3\alpha_n^2 L^{-2} \tag{27}$$

where

$$a_n = K_n^2; \quad b_n = 3K_n^2\beta_n; \quad c_n = 3K_n^2\beta_n^2 \tag{28}$$

At this point, one may seek to locate a possible extremum of the total kinetic energy subject to the fundamental constraint

$$\sum_{n=0}^{\infty}(-1)^n\alpha_n = 1 \tag{29}$$

To make further headway, the method of Lagrangian multipliers may be conveniently employed by first defining the constrained energy function

$$g = E_V + \lambda\left[\sum_{n=0}^{\infty}(-1)^n\alpha_n - 1\right] \tag{30}$$

Equation (27) can then be maximized or minimized by imposing $\nabla g(\alpha_0, \alpha_1, \alpha_2, ..., \ldots, \lambda) = 0$. Specifically, one puts

$$\nabla g(\alpha_n, \lambda) = 0 \quad n = \{0, 1, 2..., \infty\} \tag{31}$$

Subsequently, the constrained energy function may be differentiated with respect to each of its variables to obtain

$$\frac{\partial g}{\partial \alpha_n} = \tfrac{1}{6}L^3\left(2a_n\alpha_n + b_n L^{-1} + 6\alpha_n L^{-2}\right) + (-1)^n\lambda = 0; \quad n = \{0, 1, 2..., \infty\} \tag{32}$$

$$\frac{\partial g}{\partial \lambda} = \sum_{n=0}^{\infty}(-1)^n\alpha_n - 1 = 0 \tag{33}$$

Equation (32) can be solved for $\{\alpha_n\}$ in terms of λ such that

$$\alpha_n = -\frac{6(-1)^n\lambda L^{-3} + b_n L^{-1}}{2\left(a_n + 3L^{-2}\right)} \tag{34}$$

The outcome is then substituted into Eq. (33) to retrieve

$$\lambda = -\frac{2L^3 + L^2\sum_{n=0}^{\infty}(-1)^n b_n\left(a_n + 3L^{-2}\right)^{-1}}{6\sum_{n=0}^{\infty}\left(a_n + 3L^{-2}\right)^{-1}} \tag{35}$$

Table 1. Sidewall injection sequence and kinetic energy density for several injection profiles

$u_0(y)$	$\{\alpha_n\}$	$\mathscr{E}$
0	$\dfrac{8\sqrt{3}(-1)^n L}{(2n+1)^2\pi^2 L^2+12}\coth\left(\dfrac{\sqrt{3}}{L}\right)$	$\dfrac{1}{L\sqrt{3}}\coth\left(\dfrac{\sqrt{3}}{L}\right)$
u_c	$\{\alpha_n\}_{\text{inert}}$	$\mathscr{E}_{\text{inert}}+\dfrac{u_c(u_c+L)}{L^2}$
$u_c(1-y^2)$	$\{\alpha_n\}_{\text{inert}}-\dfrac{8L(-1)^n u_c}{(2n+1)^2\pi^2}$	$L(1+Lu_c)^2\mathscr{E}_{\text{inert}}-\frac{1}{15}\left[-8L^{-2}u_c^2+5u_c^2(1+L^2)+10Lu_c\right]$

When λ is inserted back into Eq. (34), the general solution for $\{\alpha_n\}$ is extracted. This is

$$\alpha_n=\frac{(-1)^n S_1-b_n S_2}{\left(a_n+3L^{-2}\right)S_3} \tag{36}$$

where

$$\begin{cases} S_1=2+L^{-1}\sum_{i=0}^{\infty}(-1)^i b_i\left(a_i+3L^{-2}\right)^{-1} \\ S_2=L^{-1}\sum_{i=0}^{\infty}\left(a_i+3L^{-2}\right)^{-1}=\dfrac{1}{2\sqrt{3}}\tanh\left(\dfrac{\sqrt{3}}{L}\right) \\ S_3=2LS_2=\dfrac{L}{\sqrt{3}}\tanh\left(\dfrac{\sqrt{3}}{L}\right) \end{cases} \tag{37}$$

With the determination of $\{\alpha_n\}$, the total energy given by Eq. (27) is at hand. In certain cases, $\{\alpha_n\}$ is amenable to closed form as shown in Table 1 for inert, uniform and Poiseuille injection. Furthermore, given that the Taylor model is semi-infinite, it is useful to introduce a suitable form of energy density such as $\mathscr{E}=E_V/L^3$. Closed form expressions for the kinetic energy density are given in Table 1. Then by plotting $\mathscr{E}$ versus L in Fig. 2, one is able to assess the energy requirements associated with several standard headwall injection profiles. It can thus be seen that, for $u_c=1$, the headwall injection profiles that are accompanied by the most kinetic energy are, in descending order, the uniform, Poiseuille, Berman (half-cosine), and inert solutions. One also finds that, as the length of the chamber is increased at fixed height, $\mathscr{E}$ approaches a constant asymptotic value of $\mathscr{E}_\infty^- = 1/3 \simeq 0.334$ for each of the headwall injection patterns. A critical aspect ratio L_{cr} can therefore be conceived beyond which the kinetic energy varies by less than 7.5% from its final asymptotic value $\mathscr{E}_\infty^-$. The choice of a 7.5% variation is dictated by the slow monotonic decay of the kinetic energy density function shown in Fig. 2. Although the slope slips to 1% rather rapidly, its progression to the asymptotic value is exceedingly slow. For a chamber with $L \geq L_{cr}$, one may safely assume an infinitely long chamber in evaluating Eq. (36), thereby achieving a substantial reduction in complexity. In practice, when the headwall injection velocity is of order unity, as in the case of solid rocket motors (SRMs), the critical aspect ratio is relatively low. For example, using $u_c = 1, \frac{1}{2}\pi, 3/2$ (i.e. assuming that headwall and sidewall grain surfaces are burning at equal rates, so that $U_c = U_w$),[4] L_{cr} can be calculated to be 41.29, 41.34, and 41.33 for the uniform, Berman, and Poiseuille solutions, respectively. It is interesting to note that the critical length in this case is almost twice as large as that for the cylindrical case.[5]

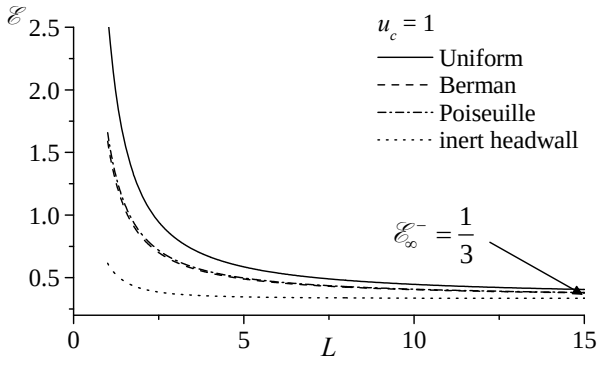

Figure 2. Variation of the total kinetic energy for each of the classic headwall injection profiles. Results are shown for a headwall-to-sidewall injection velocity ratio of unity.

A simple case may be illustrated for a slab rocket chamber with an aspect ratio that exceeds L_{cr}. By letting $L \to \infty$, Eq. (36) reduces to

$$\alpha_n = (-1)^n \left(a_n \sum_{i=0}^{\infty} a_i^{-1} \right)^{-1} = \frac{8(-1)^n}{\pi^2 (2n+1)^2} \tag{38}$$

This simple relation identically satisfies the fundamental constraint expressed through Eq. (29). More importantly, Eq. (38) establishes that, for long channels, $\{\alpha_n\}$ becomes independent of the headwall injection sequence $\{\beta_n\}$. This grants $\{\alpha_n\}$ a universal character, namely, specificity that is independent of the imposed fore-end profile. To explain this behavior, two reasons may be offered. Firstly, the effect of headwall injection diminishes so rapidly in the downstream direction that it becomes negligible in sufficiently long channels. Such depreciation is corroborated by the results obtained in previous studies that consider the fundamental Taylor type solution with arbitrary injection.[4,9] Secondly, it may be remarked that sidewall injection constitutes the essential driver for Taylor's model. At the outset, any alteration to the sidewall mass addition will significantly change the solution. Conversely, altering headwall injection has no bearing on the ensuing profile.[10] Given sufficient distance from the headwall, all flows will eventually evolve to the self-similar form obtained with no headwall injection.

C. Least Kinetic Energy Solution

While the Lagrangian optimization allows us to locate the problem's extremum, it does not provide a hint on whether the result corresponds to a maximum or a minimum. The simplest way to obtain this information is to substitute Eq. (38) into Eq. (27) and compare the energy content of the new solution with that of Taylor's. Our method exposes the solution that expends the least kinetic energy. The minimum energy solution for the inert headwall case can thus be written as

$$\psi(x,y) = \frac{8}{\pi^2} x \sum_{n=0}^{\infty} \frac{(-1)^n}{(2n+1)^2} \sin\left[\tfrac{1}{2}(2n+1)\pi y\right] \tag{39}$$

For other injection profiles, $\{\alpha_n\}$ remains the same while $\{\beta_n\}$ varies according to the imposed fore-end flow distribution. The streamfunctions and axial velocities with least kinetic energy are posted in Table 2 using four different headwall injection patterns. The normal velocity component is the same regardless of the headwall injection profile. This is given by

$$v(y) = -\frac{8}{\pi^2} \sum_{n=0}^{\infty} \frac{(-1)^n}{(2n+1)^2} \sin\left[\tfrac{1}{2}(2n+1)\pi y\right] \tag{40}$$

Other possible solutions could be just as easily obtained by direct substitution and evaluation of Eqs. (36), (20), and (19). Corresponding streamlines are illustrated in Fig. 3 for zero headwall injection as well as for uniform, Berman (half cosine), and Poiseuille configurations. Using solid lines to denote the traditional Taylor's, the solutions with least kinetic energy are shown using broken lines. These exhibit steep curvatures that are reminiscent of those associated with turbulent or compressible flow motions.[11]

Table 2. Mean flow streamfunction and axial velocity with least kinetic energy

Headwall injection $u_0(y)$	Stream function $\psi^-(x,y)$	Axial velocity $u^-(x,y)$
0	$\frac{8}{\pi^2} x \sum_{n=0}^{\infty} \frac{(-1)^n}{(2n+1)^2} \sin\eta; \quad \eta = (n+\frac{1}{2})\pi y$	$\frac{4}{\pi} x \sum_{n=0}^{\infty} \frac{(-1)^n}{(2n+1)} \cos\eta$
u_c	$\frac{8}{\pi^2}(x+u_c) \sum_{n=0}^{\infty} \frac{(-1)^n}{(2n+1)^2} \sin\eta$	$\frac{4}{\pi}(x+u_c) \sum_{n=0}^{\infty} \frac{(-1)^n}{(2n+1)} \cos\eta$
$u_c \cos\left(\frac{1}{2}\pi y\right)$	$2\frac{u_c}{\pi} \sin\left(\frac{1}{2}\pi y\right) + \frac{8}{\pi^2} x \sum_{n=0}^{\infty} \frac{(-1)^n}{(2n+1)^2} \sin\eta$	$u_c \cos\left(\frac{1}{2}\pi y\right) + \frac{4}{\pi} x \sum_{n=0}^{\infty} \frac{(-1)^n}{(2n+1)} \cos\eta$
$u_c\left(1-y^2\right)$	$\frac{8}{\pi^2} \sum_{n=0}^{\infty} \frac{(-1)^n}{(2n+1)^2} \left[x + \frac{8u_c}{\pi^2 (2n+1)^2} \right] \sin\eta$	$\frac{4}{\pi} \sum_{n=0}^{\infty} \frac{(-1)^n}{(2n+1)} \left[x + \frac{8u_c}{\pi^2 (2n+1)^2} \right] \cos\eta$

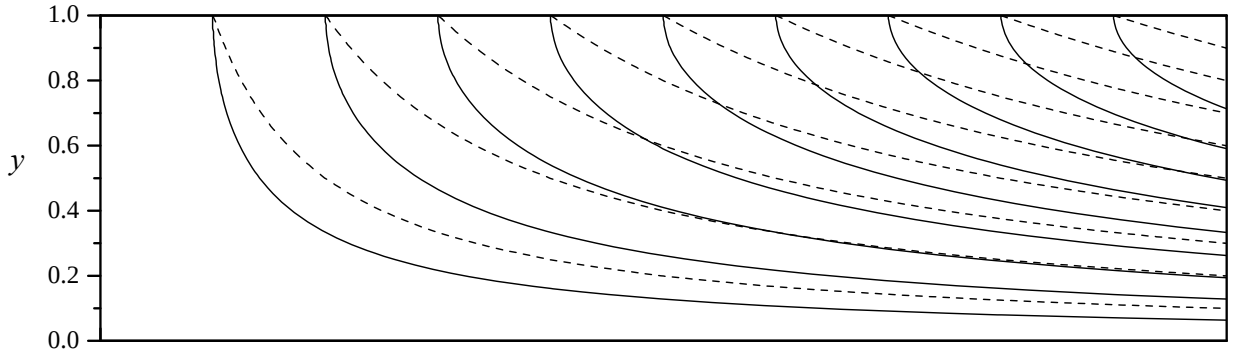

a) inert headwall

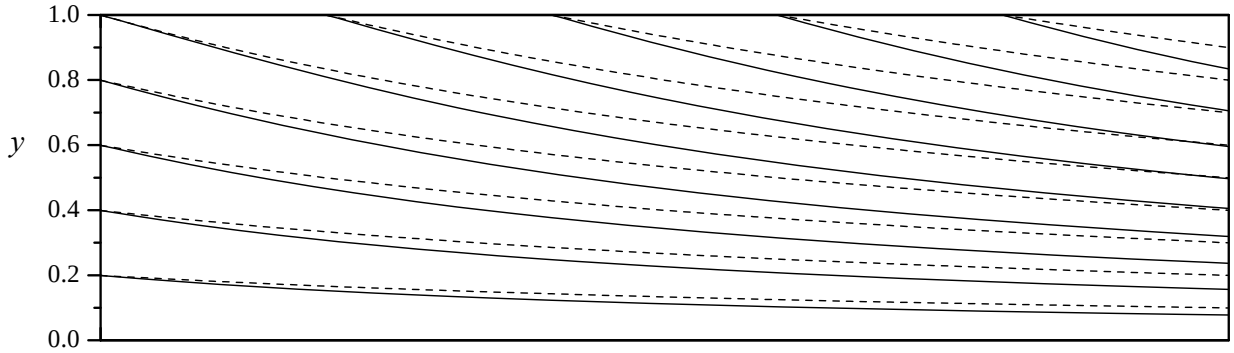

b) uniform flow

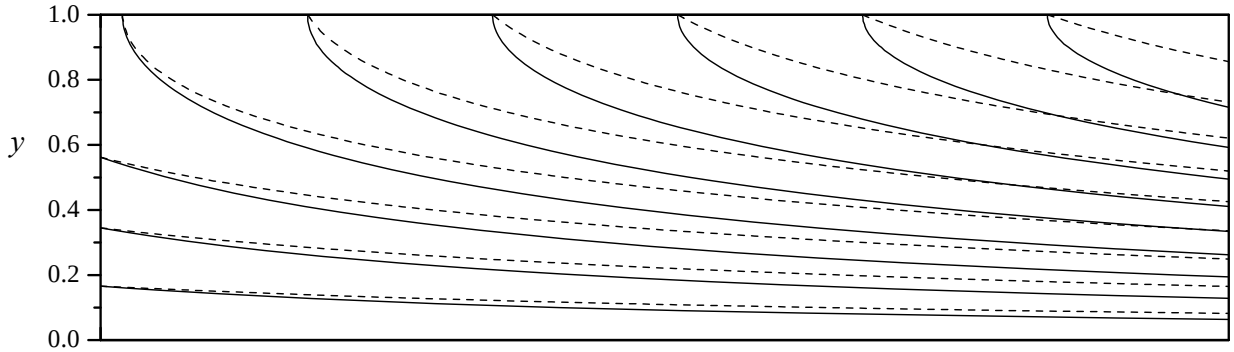

c) Berman's half cosine

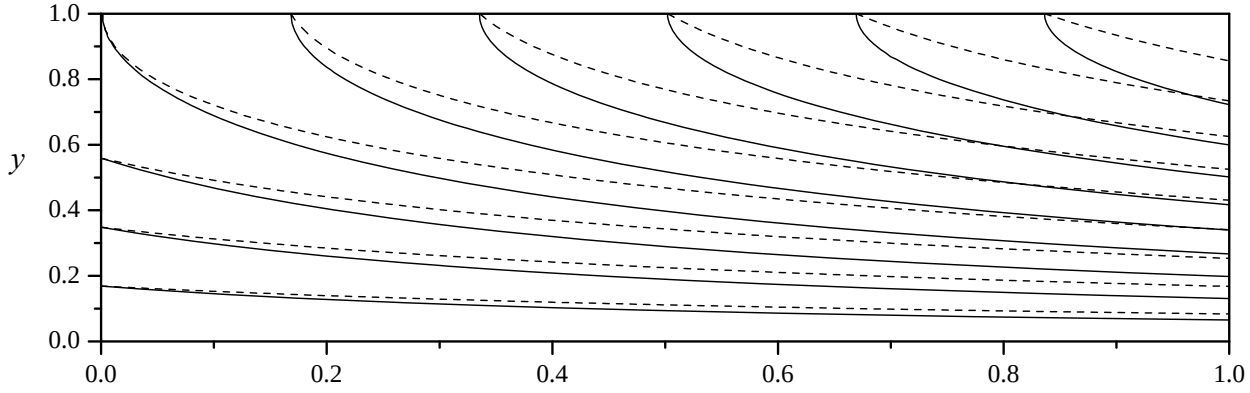

d) Poiseuille flow

Figure 3. Comparison of the Taylor (solid) streamlines and the Type I least kinetic energy solutions with steeper curvature (broken lines).

IV. Generalization

So far a Taylor type solution has been captured bearing the minimum kinetic energy that the flow may be able to sustain. It would be valuable to identify other mean flow solutions that exhibit increasing or decreasing levels of kinetic energy, specifically those leading to the flowfield with maximum energy requirement. It would also be instructive to rank the Taylor solution according to its energy content within the set of possible solutions. To this end, we consider long channels and make use of Eq. (38) as a guide. As indicated earlier, the source of flow alteration stems from sidewall injection, and thus the sidewall injection sequence $\{\alpha_n\}$ will comprise the key parameters that control the energy level for a given flowfield.

A. Type I Solutions with Increasing Energy Levels

From this standpoint, we introduce an alternative formulation for $\{\alpha_n\}$. Inspired by the form obtained through Lagrangian optimization, we note that

$$\alpha_n = \frac{8(-1)^n}{\pi^2(2n+1)^2} \sim \frac{(-1)^n A_2}{(2n+1)^2} \tag{41}$$

where $A_2 = 8/\pi^2$ can be deduced from the lateral inflow requirement given by Eq. (29). Its subscript is connected with the power of $(2n+1)$ in the denominator. In our attempt to generalize, we assume the generic Type I form

$$\alpha_n^-(q) = \frac{(-1)^n A_q}{(2n+1)^q}; \quad q \geq 2 \tag{42}$$

where $q = 2$ reproduces the state of least energy consumption. Note that the 'minus' sign in the superscript denotes energies that are lower than Taylor's. This relation can be made to satisfy Eq. (29) when

$$\sum_{n=0}^{\infty}(-1)^n \frac{(-1)^n A_q}{(2n+1)^q} = 1 \quad \text{or} \quad A_q = \frac{1}{\sum_{n=0}^{\infty}(2n+1)^{-q}} = \frac{1}{\zeta(q)(1-2^{-q})}; \quad \zeta(q) = \sum_{k=1}^{\infty} k^{-q} \tag{43}$$

where ζ is Riemann's zeta function. Note that the $q \geq 2$ condition is needed to ensure series convergence down to the vorticity. Backward substitution enables us to collect the proper form of $\{\alpha_n\}$, namely,

$$\alpha_n^-(q) = \frac{(-1)^n}{(2n+1)^q \sum_{k=0}^{\infty}(2k+1)^{-q}} = \frac{(-1)^n (2n+1)^{-q}}{\zeta(q)(1-2^{-q})}; \quad q \geq 2 \quad \text{(Type I)} \tag{44}$$

The exponent q may be dubbed the *kinetic energy power index*. With the form given by Eq. (44), one can plot the variation of the total kinetic energy versus the kinetic energy power index q. This plot is shown in Fig. 4a for an inert headwall. Interestingly, as $q \to \infty$, Taylor's classic solution is strictly recovered. In fact, using Eq. (44), it can be demonstrated that

$$\lim_{q\to\infty} \alpha_n^-(q) = \begin{cases} 1; & n = 0 \\ 0; & \text{otherwise} \end{cases} \tag{45}$$

This result identically reproduces Taylor's expression. All of the Type I solutions that can be precipitated from Eq. (44) possess kinetic energies that are lower than Taylor's. They can be bracketed between Eq. (39) and $\psi(x, y) = x\sin(\frac{1}{2}\pi y)$. In practice, all solutions with $q \geq 5$ will be Taylor-like as their energies will differ by less than 1%. The most distinct solutions correspond to $q = 2$, 3, and 4 with energies that are 81.04, 91.7, and 97.26% of Taylor's.

B. Type II Solutions with Decreasing Energy Levels

To capture solutions with energies that exceed that of Taylor's, a modified formulation for $\{\alpha_n\}$ is required. One may set

$$\alpha_n^+(q) = \frac{B_q}{(2n+1)^q}; \quad q \geq 2 \tag{46}$$

The key difference here stands in the exclusion of the $(-1)^n$ multiplier which was previously retained in Eq. (42). Unless this term is lumped into B_q, no solutions can be identified with energies higher than Taylor's. Again, the

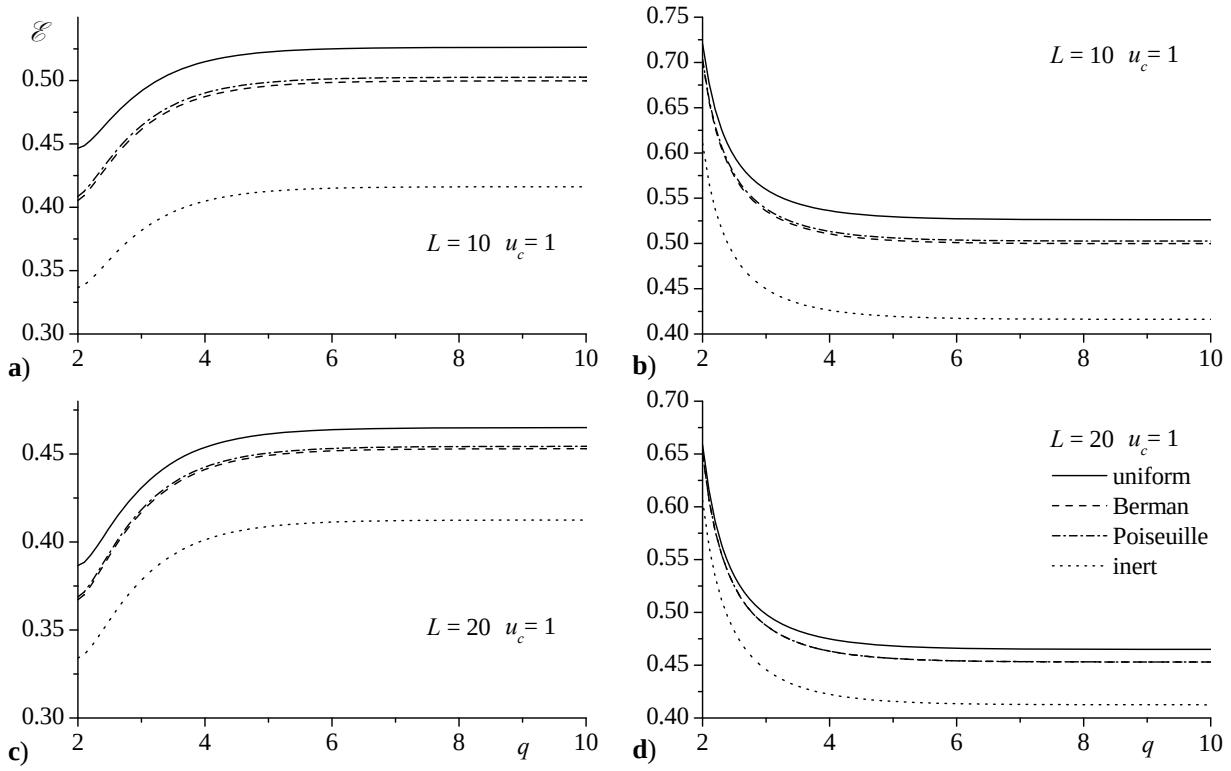

Figure 4. Total kinetic energy density in a simulated SRM chamber for either (a,c) Type I solutions (left) with increasing energy levels or (b,d) Type II solutions (right) with decreasing energy levels. Results are for L = 10 (top) and 20 (bottom).

'plus' sign in the superscript denotes energies that are higher than Taylor's. The remaining steps follow similar lines as before. Substitution into Eq. (29) unravels

$$\sum_{n=0}^{\infty}(-1)^n\frac{B_q}{(2n+1)^q}=1 \quad \text{or} \quad B_q=\frac{1}{\sum_{n=0}^{\infty}(-1)^n(2n+1)^{-q}}=\frac{4^q}{\zeta(q,\frac{1}{4})-\zeta(q,\frac{3}{4})} \tag{47}$$

where $\zeta(q,x)$ is the generalized Riemann zeta function. Following subtitution back into Eq. (46), we retrieve

$$\alpha_n^+(q)=\frac{(2n+1)^{-q}}{\sum_{k=0}^{\infty}(-1)^k(2k+1)^{-q}}=\frac{4^q(2n+1)^{-q}}{\zeta(q,\frac{1}{4})-\zeta(q,\frac{3}{4})} \quad \text{(Type II)} \tag{48}$$

It can be shown that all Type II solutions emerging from Eq. (48) dispose of higher kinetic energies than Taylor's. The variation of the solution with respect to q is illustrated in Figs. 5b and 5c. According to this form of $\{\alpha_n^+\}$, Taylor's model is recoverable asymptotically by taking the limit as $q\to\infty$. Here too, most of the solutions will exhibit energies that lie within 1% of Taylor's. The most interesting solutions are, in descending order, those corresponding to $q=2$, 3, and 4 with energies that are 47.03, 8.08, and 2.40% larger than Taylor's. When the energy level is fixed at $q=2$, a simplification follows. Catalan's constant emerges in Eq. (48), namely, in the form

$$\mathscr{C}=\sum_{k=0}^{\infty}(-1)^k(2k+1)^{-2}\simeq 0.915966 \tag{49}$$

Several Type II solutions that carry the most energy $(q=2)$ are plotted in Fig. 5 and listed in Table 3. In Fig. 5, the Type II approximations are seen to overshoot the Taylor streamline curvature for four cases corresponding to different headwall injection patterns. These cover standard configurations such as: a) inert headwall, b) uniform flow, c) Berman's half cosine, and d) Poiseuille profiles.

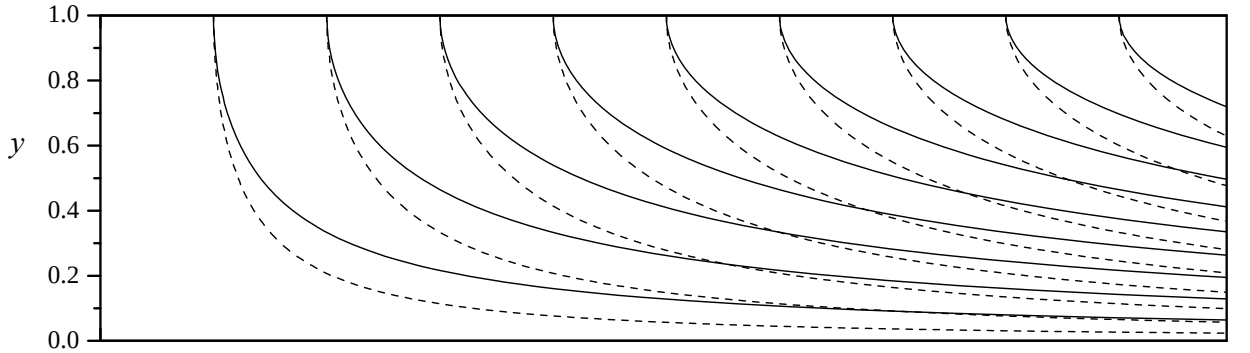

a) inert headwall

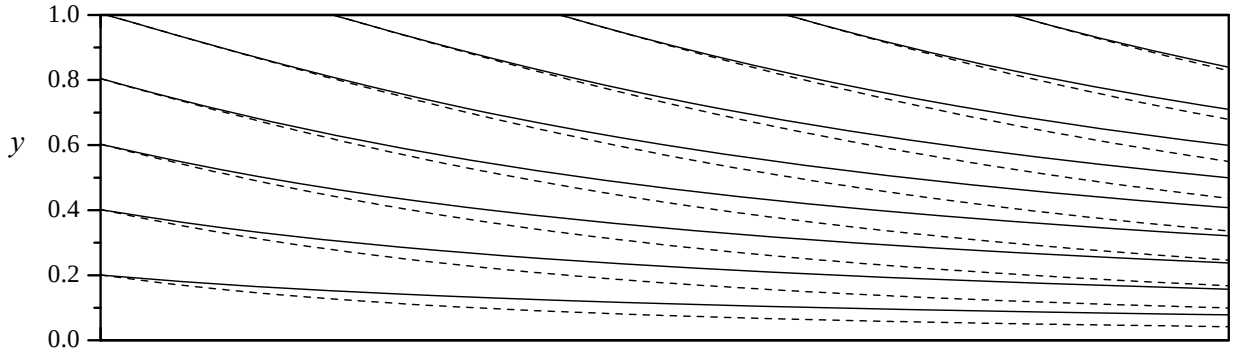

b) uniform flow

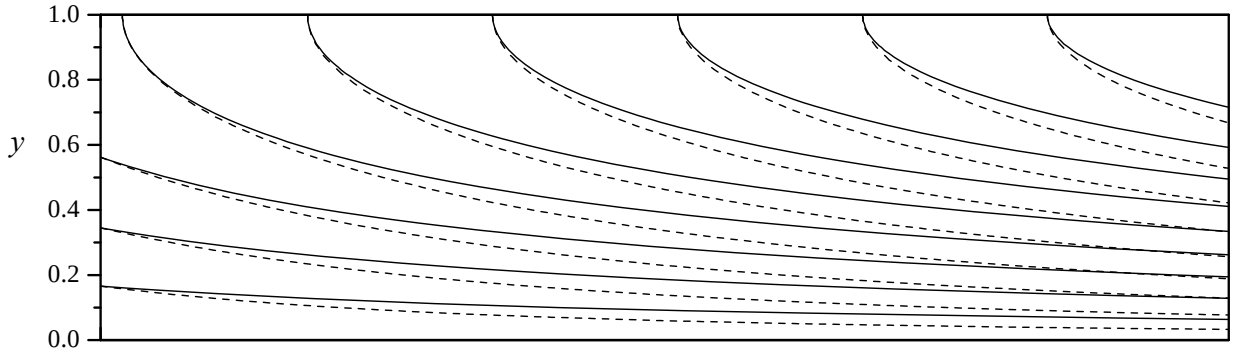

c) Berman's half cosine

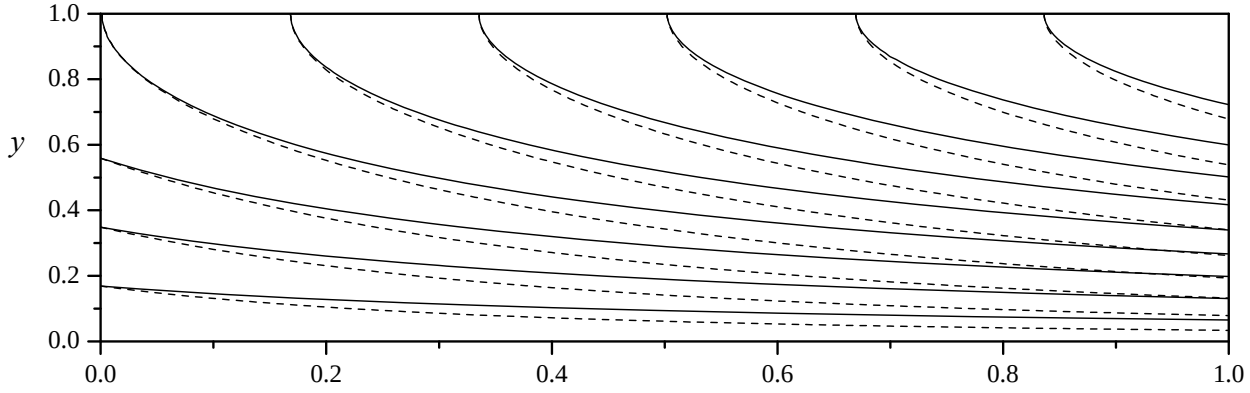

d) Poiseuille flow

Figure 5. Comparison of the Taylor (solid) streamlines and the Type II energy-maximized Taylor solutions with overshooting curvature (broken lines).

Table 3. Mean flow solutions with most kinetic energy for several headwall injection patterns

Headwall injection $u_0(r)$	Stream function $\psi^+(x,y)$	Axial velocity $u^+(x,y)$
0	$\frac{x}{\mathscr{C}}\sum_{n=0}^{\infty}\frac{\sin\eta}{(2n+1)^2}$	$\pi\frac{x}{2\mathscr{C}}\sum_{n=0}^{\infty}\frac{\cos\eta}{(2n+1)}$
u_c	$\sum_{n=0}^{\infty}\left[\frac{x}{\mathscr{C}}+\frac{8(-1)^n}{\pi^2}u_c\right]\frac{\sin\eta}{(2n+1)^2}$	$\frac{\pi}{2}\sum_{n=0}^{\infty}\left[\frac{x}{\mathscr{C}}+\frac{8(-1)^n}{\pi^2}u_c\right]\frac{\cos\eta}{(2n+1)}$
$u_c\cos\left(\frac{1}{2}\pi y\right)$	$2\frac{u_c}{\pi}\sin\left(\frac{1}{2}\pi y\right)+\frac{x}{\mathscr{C}}\sum_{n=0}^{\infty}\frac{\sin\eta}{(2n+1)^2}$	$u_c\cos\left(\frac{1}{2}\pi y\right)+\pi\frac{x}{2\mathscr{C}}\sum_{n=0}^{\infty}\frac{\cos\eta}{(2n+1)}$
$u_c\left(1-y^2\right)$	$\sum_{n=0}^{\infty}\left[\frac{x}{\mathscr{C}}+\frac{64(-1)^n u_c}{\pi^2(2n+1)^2}\right]\frac{\sin\eta}{(2n+1)^2}$	$\frac{\pi}{2}\sum_{n=0}^{\infty}\left[\frac{x}{\mathscr{C}}+\frac{64(-1)^n u_c}{\pi^2(2n+1)^2}\right]\frac{\cos\eta}{(2n+1)}$

Table 4. Vorticity with least or most kinetic energy for several headwall injection patterns

Headwall injection $u_0(y)$	Type I vorticity $\omega_z^-(x,y)$	Type II vorticity $\omega_z^+(x,y)$
0	0	$\frac{\pi^2}{8\mathscr{C}}x\csc\left(\frac{\pi}{2}y\right)$
u_c	0	$\frac{\pi^2}{8\mathscr{C}}x\csc\left(\frac{\pi}{2}y\right)$
$u_c\cos\left(\frac{1}{2}\pi y\right)$	$\frac{1}{2}\pi u_c\sin\left(\frac{1}{2}\pi y\right)$	$\frac{1}{2}\pi u_c\sin\left(\frac{1}{2}\pi y\right)+\frac{\pi^2}{8\mathscr{C}}x\csc\left(\frac{\pi}{2}y\right)$
$u_c\left(1-y^2\right)$	$2u_c y$	$2u_c y+\frac{\pi^2}{8\mathscr{C}}x\csc\left(\frac{\pi}{2}y\right)$

C. Energy Brackets

The two types of solutions obtained so far have energies that either exceed or lag that of Taylor's. Since both families converge to Taylor's as q is increased, it may be viewed as a stable saddle point to which these approximations are bound to converge. In Fig. 6, the least and most kinetic energy densities corresponding to $q=2$ are compared to Taylor's given several headwall injection shapes. Evidently, the curve obtained for Taylor's bisects the range of possible excursions in energy associated with the Type I and Type II solutions.

D. Velocity and Vorticity

As an illustration of the effect of the kinetic energy on the velocity profile, axial and radial velocity plots are shown in Fig. 7 for a channel with an inert headwall. The vorticity may be determined from

$$\omega_z=\frac{\partial v}{\partial x}-\frac{\partial u}{\partial y}=\tfrac{1}{4}\pi^2\sum_{n=0}^{\infty}(2n+1)^2\left(\alpha_n x+\beta_n\right)\sin\eta \tag{50}$$

This expression is evaluated for the least and most kinetic energy formulations $(q=2)$, as well as for the representative injection profiles considered in this work. These are provided in Table 4. A close inspection of these solutions reveals that the vorticity associated with the least kinetic energy consists solely of the vorticity contributed by headwall injection because the contribution from the sidewall, i.e. the summation term containing $\{\alpha_n\}$, is identically zero inside the channel. Mathematically, this can be written as

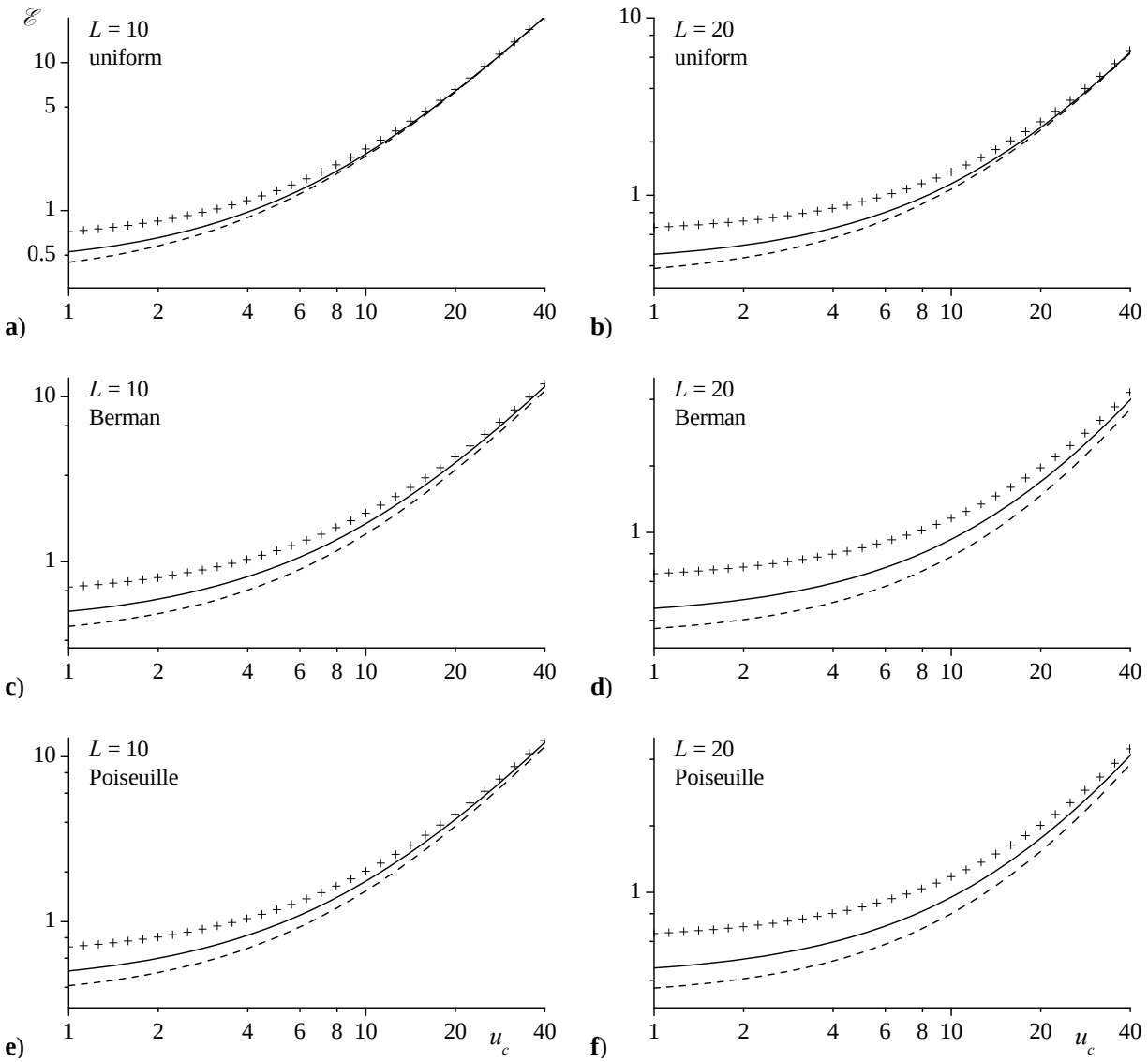

Figure 6. Total kinetic energy density for Type I and Type II solutions tailing and leading Taylor's. Results are shown for L = 10 (left) and 20 (right) given: (a,b) uniform, (c,d) Berman, and (e,f) Poiseuille headwall injection profiles.

$$\omega_z^-\left(q=2\right)=-\frac{\partial u_0\left(y\right)}{\partial y} \tag{51}$$

This relation clearly explains the absence of vorticity in the uniform injection profile given that $u_0\left(y\right)=u_c$ is strictly irrotational.

E. Asymptotic Behavior of the Kinetic Energy Density

Up to this point, the large aspect ratio approximation has been solely used in computing $\{\alpha_n\}$, but the full expression is left intact in calculating the kinetic energy. Here we compute the limit of the kinetic energy density as $L\to\infty$ for both Type I and Type II solutions. In general, provided that u_c is finite, the limit of the kinetic energy density can be expressed as

$$\mathscr{E}_\infty=\tfrac{1}{24}\pi^2\sum_{n=0}^{\infty}\left(2n+1\right)^2\alpha_n^2=\mathscr{E}_\infty^\infty\sum_{n=0}^{\infty}\left(2n+1\right)^2\alpha_n^2 \tag{52}$$

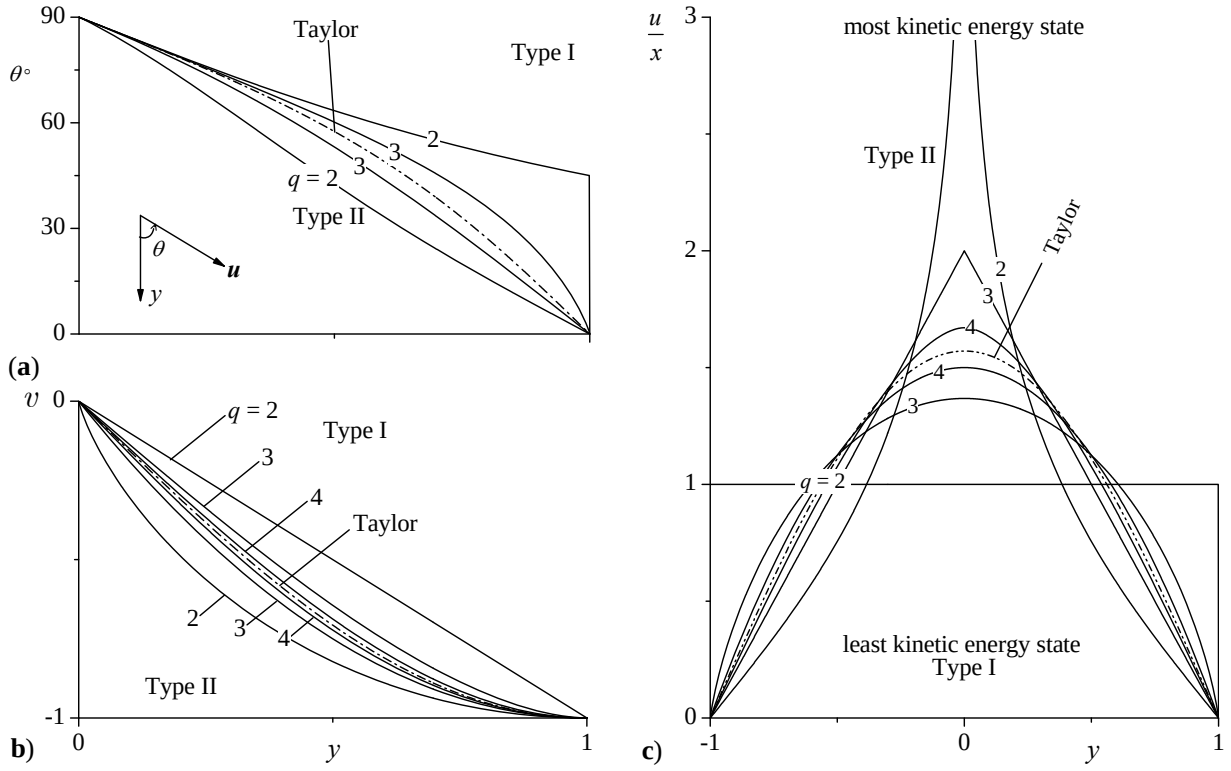

Figure 7. Effect of the energy power index on the velocity field for the flow with an inert headwall; (a) turn angle, (b) normal velocity, and (c) axial velocity.

where $\mathscr{E}_\infty^\infty \equiv \pi^2/24 \simeq 0.4112$ represents the asymptotic limit of the kinetic energy of the Taylor solution ($L \to \infty$ and $q \to \infty$). For the Type I solutions, substitution of Eq. (44) yields

$$\mathscr{E}_\infty^-(q) = \mathscr{E}_\infty^\infty \left[\sum_{k=0}^{\infty}(2k+1)^{-q}\right]^{-2} \sum_{n=0}^{\infty}(2n+1)^{2-2q} = \mathscr{E}_\infty^\infty \frac{4^q-4}{(2^q-1)^2}\frac{\zeta(2q-2)}{[\zeta(q)]^2} \tag{53}$$

In like manner, for the Type II solutions, Eq. (48) leads to

$$\mathscr{E}_\infty^+(q) = \mathscr{E}_\infty^\infty \left[\sum_{k=0}^{\infty}(-1)^k(2k+1)^{-q}\right]^{-2} \sum_{n=0}^{\infty}(2n+1)^{2-2q} = \mathscr{E}_\infty^\infty \frac{4^q(4^q-4)\zeta(2q-2)}{[\zeta(q,\frac{1}{4})-\zeta(q,\frac{3}{4})]^2} \tag{54}$$

It is interesting to note that these asymptotic limits are independent of headwall injection (u_c or β_n). Specific values of these limits are $\mathscr{E}_\infty^-(2,4,6) = (0.33, 0.40, 0.41)$ for the Type I, and $\mathscr{E}_\infty^+(2,4,6) = (0.61, 0.42, 0.41)$ for the Type II. Both types approach $\mathscr{E}_\infty^\infty$ either from below or above. Since these limits are quickly achieved as the length of the chamber is increased, they are directly applicable to simulated rocket motor flows. The energy associated with each kinetic energy power index may be inferred from Fig. 8. Note that the Taylor-Culick limit of $\mathscr{E}_\infty^\infty = 0.4112$ is practically reached by both Type I and Type II solutions with differences of less than $\left(\mathscr{E}_\infty(6) - \mathscr{E}_\infty^\infty / \mathscr{E}_\infty^\infty\right)$ 0.29% and 0.27% at $q = 6$, respectively. Given the maximum range at $q = 2$, the total allowable excursion in energy that the mean flow can undergo may be readily estimated at $\left[\mathscr{E}_\infty^+(2) - \mathscr{E}_\infty^-(2)\right] / \mathscr{E}_\infty^\infty \simeq 66\%$, an appreciable portion of the available energy.

V. Convergence

Using the absolute and ratio tests, the series solutions presented in this work are carefully checked for convergence. We find that all series converge provided that the energy power index is greater than 2. The most subtle cases correspond to the limiting solutions with $q = 2$ where differentiation is not always valid. In general, term by term differentiation may be used provided the singularity points are excluded from the domain of interest. For example, differentiation of the velocity associated with the most kinetic energy solution may be used when the centerline $(y = 0)$ is excluded. This velocity profile is depicted in Fig. 7c and represents an alternating series that

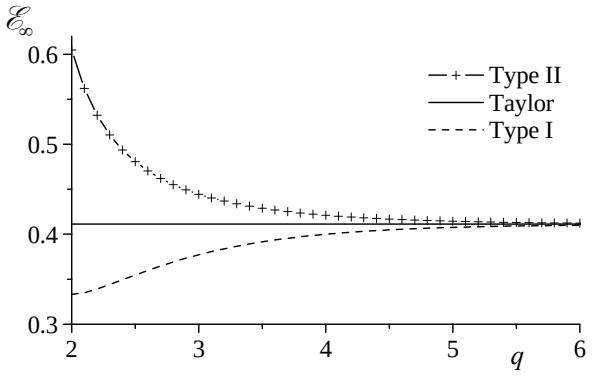

Figure 8. Asymptotic limits of the kinetic energy density for large *L* showing rapid convergence of both Type I and Type II solutions to the Taylor value of 0.4112.

diverges at the centerline. A simple remedy for avoiding the difficulties associated with term by term differentiation consists of using closed form representations of the series in question. In the interest of clarity, the Type II inert injection solution is examined. Here we start with the streamfunction

$$\psi^+(x,y) = x\sum_{n=0}^{\infty}\frac{B_q}{(2n+1)^q}\sin\left[\tfrac{1}{2}(2n+1)\pi y\right] \qquad (55)$$

The absolute convergence test may then be implemented to show that

$$\sum_{n=0}^{\infty}\left|\frac{1}{(2n+1)^q}\sin\left[\tfrac{1}{2}(2n+1)\pi y\right]\right| \le \sum_{n=0}^{\infty}\frac{1}{(2n+1)^q} \qquad (56)$$

The right-hand-side of Eq. (56) converges whenever $q \ge 2$. For the limiting case of $q = 2$, care should be taken in evaluating first and second derivatives because term-by-term differentiation cannot be applied. Instead, a closed form representation of the first derivative of Eq. (55) is obtained. At $q = 2$, we transform the infinite series into

$$u^+(x,y) = \pi\frac{x}{2\mathscr{E}}\sum_{n=0}^{\infty}\frac{\cos\eta}{(2n+1)} = \frac{\pi x}{4\mathscr{E}}\left[\tanh^{-1}\left(e^{i\frac{1}{2}\pi y}\right)+\tanh^{-1}\left(e^{-i\frac{1}{2}\pi y}\right)\right] \qquad (57)$$

Subsequent differentiation of Eq. (57) yields a closed form expression for vorticity, namely,

$$\omega_\theta^+(x,y) = \frac{\pi^2}{8\mathscr{E}}x\csc\left(\frac{\pi}{2}y\right) \qquad (58)$$

VI. Conclusions

In the past four decades, simplified models for the flow in a rocket chamber have been extensively used in the propulsion community as a benchmark venue for understanding the various flow features in a solid rocket motor. Recently, an extended form has been presented in which variable headwall injection could be accommodated in both Cartesian and cylindrical settings.[3,4] In this article, we show that for each type of headwall injection pattern and chamber aspect ratio, other solutions may be obtained, and these are accompanied by lower or higher kinetic energies that vary by up to 66% of their mean value (the fundamental Taylor solution). After identifying that $\alpha_n^- \sim (-1)^n(2n+1)^{-2}$ yields the profile with least kinetic energy, similar (Type I) solutions are unraveled in ascending order, $\alpha_n^- \sim (-1)^n(2n+1)^{-q}$; $q > 2$, up to Taylor's. The latter is asymptotically recovered in the limit as $q \to \infty$. In practice, however, most solutions become indiscernible from Taylor's for $q \ge 5$. Interestingly, those obtained with $q = 2$, 3, and 4 exhibit energies that are 19, 8.3 and 2.7% lower than their remaining counterparts when $L \to \infty$. When the same analysis is repeated using $\alpha_n^+ \sim (2n+1)^{-q}$; $q \ge 2$, a complementary family of (Type II) solutions is identified with descending energy levels. Their most notable profiles correspond to $q = 2$, 3, and 4 with energies that are 47.0, 8.1, and 2.4% higher than Taylor's when $L \to \infty$. Here too, all Type II solutions resemble the classic form which is identically regained as $q \to \infty$. Effectively, both Type I and II solutions converge to the Taylor representation when their energies are augmented or reduced, respectively. Profiles belonging to these families of solutions with $q \to \infty$ and $u_c = 1, \frac{1}{2}\pi, 3/2$ (corresponding to uniform, Berman, and Poiseuille injection) have been verified in separate work by the authors[4] using computational fluid dynamics.

Acknowledgments

This work is sponsored by the National Science Foundation. The second author wishes to acknowledge valuable discussions with Dr. Grégoire Casalis, Professor and Director of the Doctoral School of Aeronautics and Astronautics, SUPAERO, and Research Director, Department of Aerodynamics and Energetics, ONERA, Toulouse, France.

References

[1]Culick, F. E. C., "Rotational Axisymmetric Mean Flow and Damping of Acoustic Waves in a Solid Propellant Rocket," *AIAA Journal,* Vol. 4, No. 8, 1966, pp. 1462-1464.

[2]Taylor, G. I., "Fluid Flow in Regions Bounded by Porous Surfaces," *Proceedings of the Royal Society, London, Series A,* Vol. 234, No. 1199, 1956, pp. 456-475.

[3]Majdalani, J., and Saad, T., "The Taylor-Culick Profile with Arbitrary Headwall Injection," *Physics of Fluids,* Vol. 19, No. 9, 2007, pp. 093601-10.

[4]Saad, T., and Majdalani, J., "The Taylor Profile in Porous Channels with Arbitrary Headwall Injection," AIAA Paper 2007-4120, June 2007.

[5]Majdalani, J., and Saad, T., "Energy Steepened States of the Taylor-Culick Profile," AIAA Paper 2007-5797, July 2007.

[6]Apte, S., and Yang, V., "Unsteady Flow Evolution in a Porous Chamber with Surface Mass Injection. Part I: Free Oscillation," *AIAA Journal,* Vol. 39, No. 8, 2001, pp. 1577-1586.

[7]Apte, S., and Yang, V., "Unsteady Flow Evolution in a Porous Chamber with Surface Mass Injection. Part II: Acoustic Excitation," *AIAA Journal,* Vol. 40, No. 2, 2002, pp. 244-253.

[8]Wasistho, B., Balachandar, S., and Moser, R. D., "Compressible Wall-Injection Flows in Laminar, Transitional, and Turbulent Regimes: Numerical Prediction," *Journal of Spacecraft and Rockets,* Vol. 41, No. 6, 2004, pp. 915-924.

[9]Majdalani, J., "The Taylor-Culick Profile with Uniform Headwall Injection," AIAA Paper 2005-4534, July 2005.

[10]Majdalani, J., and Vyas, A. B., "Inviscid Models of the Classic Hybrid Rocket," AIAA Paper 2004-3474, July 2004.

[11]Majdalani, J., "The Compressible Taylor-Culick Flow," AIAA Paper 2005-3542, July 2005.